Renewable Energy 224 (2024) 120170

Contents lists available at ScienceDirect

Renewable Energy

journal homepage: www.elsevier.com/locate/renene

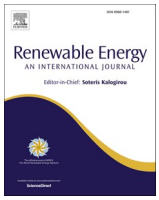

Modeling of the evolution of the porous structure during a physical activation process for the production of activated biocarbon: A novel low conversion approach

Javier Pallarés Ranz *, Antonia Gil, Cristóbal Cortés, Inmaculada Arauzo

Universidad de Zaragoza- IUI Mixto CIRCE, Campus Río Ebro, Mariano Esquillor Gómez, 15, 50018, Zaragoza, Spain

ARTICLE INFO

Keywords:
Activated biocarbon
Physical activation
Random pore model
Pore evolution model

ABSTRACT

Many experimental studies have shown the feasibility of using biomass precursors to produce activated carbon, often improving the properties obtained from traditional materials. However, hardly any models focus on the development of porosity during the process. Among the so-called pore models, the random pore model (RPM) is the most popular and accurately predicts the evolution of the porous structure due to pore growth and coalescence. However, in activation processes with a low degree of conversion, in which pore formation is the dominant mechanism, the RPM does not correctly predict the evolution of the specific surface area since it does not consider the appearance and creation of new porosity. In this work, a new model is proposed that predicts the specific surface area created due to the formation of new pores. Subsequently, it is combined with the determination of the variation of the specific surface area predicted by the RPM due to the growth and coalescence of existing pores. The validation of the new pore evolution model with activated carbon samples obtained at different conversions shows that the model proposed adequately predicts the specific surface area and pore distribution evolution throughout the activation process.

1. Introduction

Renewable energy intermittency and the need for energy storage are crucial in the European Union's roadmap towards a sustainable energy future by 2050 [1]. Solar and wind power generation fluctuates with weather patterns and other natural factors. This situation creates imbalances between electricity generation and demand, leading to grid instability and reliability issues. Developing advanced energy storage technologies capable of efficiently handling large-scale renewable energy storage is necessary. This includes emerging technologies closely related to applications of activated carbon (AC) materials such as hydrogen solid-state storage systems, thermal energy storage on phase change materials and batteries, and supercapacitor energy storage systems [2,3].

Hydrogen solid-state storage through adsorption on AC materials has been revealed to be an economical, safe, and promising alternative for energy storage systems. It can be effective across a wide range of temperatures and pressures, providing flexibility for different applications, and it is a reversible process with fast adsorption and desorption kinetics allowing for the efficient storage and release of hydrogen as needed on hydrogen-based energy systems such as fuel cells or hydrogen-powered vehicles [4–6].

Activated carbon can also enhance the overall thermal performance of energy storage systems based on phase change materials (PCM). By dispersing activated carbon particles throughout the PCM matrix, the high thermal conductivity of activated carbon facilitates the efficient transfer of heat within the PCM, improving its overall thermal performance and leading to faster charging and discharging rates. By varying the type, size, and concentration of activated carbon particles, the phase change temperature and latent heat of the PCM can be tailored to specific applications, optimizing energy storage and release characteristics [7–10].

Finally, activated carbon can be used as an electrode material in energy storage devices such as batteries and supercapacitors. The high surface area of AC provides plenty of space for the adsorption and desorption of ions, allowing for efficient energy storage and rapid charging/discharging cycles. AC-based supercapacitors offer high power density, fast response times, and long cycle life, making them attractive for applications that require quick bursts of energy or frequent cycling [11–13].

Activated carbon, mainly manufactured from coal, can also be

* Corresponding author.
E-mail address: jpallare@unizar.es (J. Pallarés Ranz).

https://doi.org/10.1016/j.renene.2024.120170
Received 28 August 2023; Received in revised form 8 January 2024; Accepted 15 February 2024
Available online 16 February 2024

Nomenclature

A_N	height of the Gaussian curve's peak (m^2/g nm)
D_R	reaction surface fractal dimension
D_0	initial reaction surface fractal dimension
E_a	activation energy (kJ/mol)
f(X)	conversion model
k	kinetic rate constant (min^{-1})
k_0	preexponential factor (min^{-1})
L_E	total length per unit volume (m/m^3)
m	mass of char at time t (g)
m_0	initial mass of char (g)
m_{ash}	mass of ash (g)
n	order of reaction
P_{CO2}	partial pressure of reacting gas CO_2 (kPa)
R_u	universal gas constant (kJ/mol K)
r_p	pore radius (m)
r_{pm}	mean pore radius (m)
r_{pm0}	initial mean pore radius (m)
S	surface area per unit weight (m^2/g)
S_0	initial surface area per unit weight (m^2/g)
S_{E0}	initial surface area per unit volume (m^2/m^3)
T	temperature (K)
t	time (min)
V	pore volume per unit weight (cm^3/g)
V_{E0}	initial pore volume per unit volume (m^3/m^3)
X	conversion of carbon

Greek symbols

ΔS_{fp}	variation of specific surface area due to the formation of new pores (m^2/g)
ΔS_{rpm}	variation of specific surface area due to pore growth and coalescence (m^2/g)
β	heating rate (K/min)
μ_N	mean of the Gaussian function (nm)
ρ_s	density of the particle (g/cm^3)
ρ_0	initial density of the particle (g/cm^3)
ρ_{ash}	ash density (g/cm^3)
σ	molecule radius around a cylindrical pore
σ_N	standard deviation of the Gaussian function (nm)
φ	ratio of formation of new pores to the total variation of the specific surface area
ψ	structural parameter

obtained from other carbonaceous sources, including biomass. The renewable nature of biomass and, its high availability and low cost, make activated biocarbon a widely accessible material with great interest and potential for research and development.

Many experimental studies have shown the feasibility of using biomass precursors to produce activated carbon, often improving the properties obtained from traditional materials [14]. However, there are hardly any models that focus on the development of the porosity during the process, so that is possible to predict the final properties that characterize the adsorption capacity of activated carbon from the properties of the precursor material and the conditions of the activation process. A model that predicts the evolution of the porous structure has a highly practical significance. First, it allows for predicting the conversion behavior and final properties of activated carbon obtained from biomass material, thus its possible end uses, saving many costs in direct experimentation. Consequently, it also allows extending this study to other biomass materials, promoting the search for new renewable precursors. Finally, a model from first principles can be integrated with models of full-scale reactors to become a valuable tool to optimize the process conditions in industrial plants for a particular feedstock, improving the fuel flexibility and the energy efficiency of the process.

Traditionally, solid fuel reaction models, mainly corresponding to combustion and gasification processes, are focused on determining the degree of conversion, rather than the evolution in the morphology and intrinsic structure of the particle.

In the heterogeneous gas-solid reactions that occur in the char's gasification, the particle's porous structure plays an essential role in its conversion. This is even more important in solids with a large specific surface area characterized by a high microporosity. In the early stages, at low conversions, the specific surface area of the particle increases due to the formation of new pores, mainly corresponding to closed pores blocked by condensable species deposited during carbonization and the growth of existing pores. This growth is not permanent, reaching a maximum from which the specific surface area and the reactivity of the char drastically decrease due to the coalescence of the pores.

This behavior, experimentally evidenced, is not described in popular solid reaction models such as the volume reaction model (VRM), hybrid model (HB), or the shrinking core reaction model (SCRM), which present a monotonically decreasing reactivity compatible with a continuous decrease in the specific surface area of the particle with conversion. That is why, alternative models, commonly known as pore models, have been proposed since the mid-twentieth century. Pore models attempt to mathematically describe the porous structure of the particle and its evolution during conversion [15–27].

Among them, the random pore model (RPM) is the most widely used reaction model in the literature. On the one hand, it describes the porous structure through a pore size distribution and structure-related variables such as pore volume, specific surface area, and total length of the pores, taking into account the superposition of the pores. On the other hand, the model describes the porous structure evolution during the conversion due to the mechanisms of growth and coalescence of the pores by introducing a pore structural parameter ψ.

Despite its popularity, it has been shown that the RPM fails to predict when the maximum reactivity is reached for conversions above 0.393, characteristic, for example, of catalytic gasification processes [28]. Consequently, several authors have presented modified versions of the RPM that allow a more accurate prediction in the last stages of conversion by varying the structural parameter ψ with reaction or by introducing additional experimentally adjusted parameters [29–33]. Also, at low conversion levels, which are characteristic of activation processes, there are hardly any models of the evolution of the porous structure. Almost as an exception, the recent work by Colomba et al. [34] presents a model that predicts yield and total surface area based on the assumption that activation deepens but does not widen the pores.

In this context, to make up for the scarcity of models focused on the progress of the particle porosity, the main objective of this work is the development and validation of a reaction model, which allows predicting not only conversion but also the evolution of the porous structure (surface area, pore volume, and pore size distribution) of a biomass-derived carbonaceous material depending on its physicochemical properties and on the conditions in which the physical activation process takes place.

To this purpose, different conversion models that describe the changes in the physicochemical properties of the char have been considered: VRM (volume reaction model), SCRM (shrinking core reaction model), HM (hybrid model), and RPM (random pore model). From the experimental validation of the conversion models, it is concluded that although RPM is the most accurate model predicting the solid conversion, the RPM fails to predict the evolution of the specific surface area during activation. Throughout this manuscript, the causes

for this behavior are analyzed, showing for the first time that for CO_2 activation processes with a low conversion level and dominated by the formation of new micropores, RPM is not adequate to determine the evolution of the specific surface area.

Therefore, a new model has been developed based on the specific surface area created due to the formation of new pores at the early stages of conversion. Then, it is combined with determining the variation of the specific surface area predicted by the RPM due to the growth and coalescence of existing pores. The new pore evolution model is validated with the values obtained experimentally on the activated biocarbon samples of a specific low-cost biomass (barley straw) at different conversion times in a laboratory quartz tubular reactor. The validation shows that the model proposed adequately predicts the evolution of the specific surface area throughout the activation process.

Finally, the model is completed by determining the pore size distribution from the specific surface area calculated for a particular conversion. The case in which changes in the size of the pores are small in relation to the change of the specific surface area (so that changes in the distribution of pore sizes are neglected) is considered, along with the most general case in which pore growth and coalescence begin to be significant.

2. Materials and methods

The validation of the model has been carried out through an experimental campaign using barley straw as a precursor material for the production of activated carbon through a physical activation process in two stages: carbonization with nitrogen and activation with carbon dioxide in an externally heated quartz tubular reactor.

Barley, the main crop in Spain, is present throughout the whole territory and, as reported in previous studies [14], exhibits favorable characteristics for producing high-quality activated carbon at low cost. Moreover, discounting cattle feeding, livestock beds, and energy production, 15–50 % of the waste barley straw is unused. Therefore, its usage as an AC precursor would reduce the amount of waste, creating further value and ultimately bringing a circular economy around this biomass residue. Table 1 and Table 2 present, respectively, proximate and ultimate, and ash composition analysis of the studied biomass. It can be observed that barley straw presents a low ash and a high volatile content, which favors a more significant development and evolution of the porous structure. On the other hand, ash composition analysis shows a high presence of Si, K, Ca, and Mg. It is well known that alkaline and alkaline-earth metals act as catalysts for the C(s)-CO_2 reaction, especially at high conversion levels. In contrast, Si and Al are inhibitors, causing agglomeration at high temperatures and blocking this catalytic effect. Considering the high Si concentration in this specific biomass, it may be insignificant if there is a catalytic effect on the C(s)-CO_2 reactivity.

The tests have been conducted in the experimental rig shown in Fig. 1. The central part of the rig is a horizontal tubular furnace heated by resistances (Nabertherm R 170/1000/12), inside which a cylindrical quartz reactor of 1730 mm long and 162 mm internal diameter is located. The installation is completed with the gas inlet line with two independent valves that regulate the gases used in the process: nitrogen and carbon dioxide, both coming from compressed gas cylinders. On the other hand, a condenser is installed in the gas exit line, allowing it to cool down and separate the water and tars formed. After this condenser, the gases pass through a coalescing filter where the possible humidity and the remaining tar mist are retained. Pressure and temperature measurements in both lines, flow rate meters, and a gas chromatograph (Varian 490-GC PRO) are also available.

Table 1
Proximate and ultimate analysis (% wt. Dry basis).

Moisture	UNE EN 14774-2	9.0
Volatiles	UNE EN 15148	77.2
Fixed Carbon	by difference	17.3
Ash	UNE EN 14775	5.5
C	UNE EN 15104	45.4
H	UNE EN 15104	6.1
O	by difference	41.9
N	UNE EN 15104	0.7
S	UNE EN 15289	0.07
Cl	UNE EN 15289	0.3

Table 2
Major and minor elements in ash at 550 °C (% wt. Dry basis) (UNE EN 15290).

Element	% wt	Element	% wt
Al	0.082	**Na**	0.50
Ba	0.021	**P**	1.3
Ca	7.2	**S**	1.1
Fe	0.42	**Si**	21.0
K	18	**Sr**	0.022
Mg	2.0	**Ti**	0.046
Mn	0.054	**Zn**	0.019

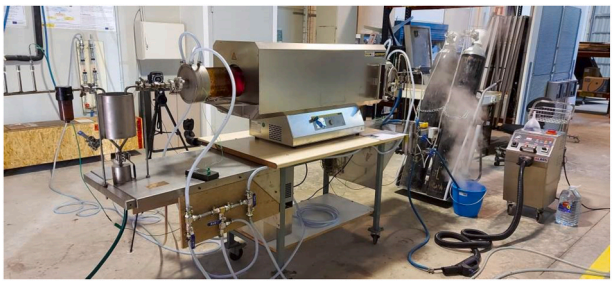

Fig. 1. Test facility used for the model validation test campaign.

The tests in the reactor have been carried out for the optimized conditions of the activation process for barley (Table 3), varying in each test the activation time between 0 and 75 min to achieve different degrees of conversion and the development of the porous internal structure.

The general experimental procedure followed for running the tests is detailed below. In each test, approximately 170 g of precursor material is prepared on two quartz sample vessels, previously ground to a size range between 0.045 and 0.5 mm, and dried in a drying oven at 105 °C to eliminate the remaining moisture and thus avoid condensation during the experiments. Once the sample holders are introduced into the reactor, and before starting the heating program, a flow of nitrogen from the compressed gas cylinder is passed through the installation to eliminate the presence of oxygen and ensure an inert atmosphere. Then, the pyrolysis and activation programs are completed according to the test conditions defined in Table 3. The switch of the nitrogen flow with that corresponding to the activating agent is carried out once the activation temperature is reached. Once the program is completed, the installation is cooled down in an inert nitrogen atmosphere.

The validation of the model is performed on the activated carbon samples obtained from the experimental test campaign conducted in the tubular reactor in terms of weight loss due to activation, BET-specific surface area, total pore volume, and pore size distribution, depending

Table 3
Operation conditions during activation tests.

Carbonization				Activation			
N_2 (cm^3/min)	T (°C)	β (°C/min)	t (min)	CO_2 (cm^3/min)	T (°C)	β (°C/min)	t (min)
2500	500	10	60	2500	800	10	0 to 75

on the degree of conversion achieved. Accordingly, the corresponding measurements and characterization analysis of the activated carbon samples are conducted after the completion of the tests.

The conversion term (X_{act}) refers to the reacted mass fraction calculated according to equation (1), which exclusively corresponds to the activation stage.

$$X_{act} = \frac{m_0 - m}{m_0 - m_{ash}} \quad (1)$$

where m_0 is the initial mass of the activation stage, m is the mass at the end of the test, and m_{ash} is the mass of the mineral matter content.

To determine the BET surface area, total volume porosity, and microporosity of each activated carbon sample, the N_2 adsorption isotherm at 77 K was determined by gas sorption analyzer ASAP 2020 (Micromeritics). Adsorption data were obtained over the relative pressure, P/P_0, ranging from 10^{-3} to 0.99. The samples were degassed at 200 °C under vacuum for 5 h. The surface area, S_{BET}, was calculated using the BET (Brunauer, Emmett, and Teller) equation. The total pore volumes were estimated to be the liquid volume of adsorbate (N_2) at a relative pressure of 0.99. The cross-sectional area of a nitrogen molecule was taken as 0.162 nm^2. In addition, the t-plot method was applied to calculate the micropore surface area and volume. Pore size distributions and mean pore radius r_{pm} were obtained using the DFT (Density Functional Theory) method.

Additionally, helium pycnometry has been used to determine the true density ρ_s of the activated samples using the Micromeritics ACCUPYC helium pycnometer at a temperature of 30 °C. Samples were previously dried at 130 °C in a vacuum oven to eliminate moisture and other adsorbed gases.

Table 4 shows the results of mass loss, conversion, BET surface area, and total pore and micropore volume obtained in the tests.

It should be noted that time zero (t = 0 min) in the tests is when CO_2 starts to flow into the reactor, once the set point temperature for the activation stage (800 °C) has been reached. For the volumetric flow of the activating agent established in the tests (2500 cm^3/min STP), a stabilization period of 15 min for filling and homogenizing the atmosphere in the reactor has been estimated, corresponding to tests 1 to 3. This is evidenced in Table 4, obtaining a decrease of the char sample mass due to the completion of the release of volatiles at 800 °C but a very low development of porosity and specific surface area in these tests. Consequently, for the validation of the reaction model, the start of the activation process, zero conversion reference, has been established as test 3.

These analyses were complemented with proximate and ultimate analysis, X-ray fluorescence and induced coupled-plasma optical emission spectroscopy to determine the elements present in the sample, X-ray diffraction analysis to determine the crystallographic structure of samples, SEM/EDX microscopy to examine the surface morphology and elemental composition of samples and ATR-FTIR spectroscopy, X-ray photoelectron spectroscopy and Boehm titration method to determine the surface functional groups on activated carbon. Results and discussion on these tests are out of the scope of model validation.

Table 4
Activation test results: mass loss and physisorption analysis.

Test	$t_{activation}$ (min)	m_0 (g)	m_f (g)	X_{act} (%)	S_{BET} (m^2/g)	V_{Tpores} (cm^3/g)	$V_{micropore}$ (cm^3/g)
1	0	170.24	45.87	0.00	4.5	0.0145	0.0003
2	7.5	170.41	44.67	3.79	3.3	0.0068	0.0010
3	15	170.48	43.63	6.52	11.6	0.0113	0.0045
4	25	170.69	42.77	8.61	110	0.0545	0.0447
5	35	170.54	41.35	12.56	174	0.0837	0.0710
6	45	170.40	39.89	16.31	230	0.1070	0.0922
7	55	170.25	39.82	17.18	244	0.1144	0.1002
8	65	170.98	39.58	17.91	225	0.1071	0.0924
9	75	170.43	37.03	23.86	290	0.1353	0.1182

Finally, to determine the kinetic parameters of the activation process, isothermal differential thermogravimetry tests have been carried out at five different temperatures (700, 750, 800, 850, and 900 °C) in a CO_2 atmosphere using the thermal gravimetric analyzer Netzsch TG 209F1 Libra following the procedure that reproduces the conditions of the activation tests in the laboratory: the sample (8–10 mg) is heated up at a rate of 10 °C/min to a temperature of 500 °C in an inert N_2 atmosphere. Next, the temperature is maintained at 500 °C for 1 h to complete the carbonization stage. After this period, the sample continues to be heated at a rate of 10 °C/min to the setpoint temperature for the activation process, also in an inert N_2 atmosphere. Finally, the reactive process with CO_2 at constant temperature is completed until the total conversion of the sample.

3. Model definition, validation, and discussion

Based on the particular characteristics of the activation process to be modeled: atmospheric reactor, isothermal conditions at moderate temperatures (700–800 °C), CO_2 atmosphere (100%), char particle size (<0.5 mm), and porosity and initial specific surface area of the char consistent with the preceding carbonization process, the following hypotheses have been considered in the model.

- Char particles of spherical geometry, with an initial porous structure, developed during the preceding carbonization stage.
- The porous structure is consistent with the RPM [23–25]. It presents cylindrical pores with smooth walls and random intersections, which are isotropically distributed throughout the particle. The pores follow a size distribution $f(r_p)$, and the porous structure is characterized based on the main parameters: total pore length per volume unit L_{E0}, total surface area per volume unit S_{E0}, and total pore volume per unit of volume V_{E0}.
- Negligible diffusional resistance. For the conditions of the CO_2 activation process in this work with temperatures below 800 °C and a mean particle size under 200 μm characteristic of the kinetic control regime (zone I), Thiele modulus values below 0.2 have been obtained, confirming that the influence of diffusion phenomena is negligible [35–39]. Consequently, the hypothesis of a purely kinetic regime is assumed in the modeling.
- A first-order reaction kinetics is assumed for the gasifying agent. In the kinetic regime, for a high and practically constant CO_2 concentration, the influence of the partial pressure of CO_2 does not have a significant effect. It can be integrated into the experimental determination of the pre-exponential factor.
- The inhibitory effect of CO is not considered. This effect is only significant at very high temperatures, which is characteristic of entrained flow gasifiers (1200–1500 °C), and with high partial pressures of CO_2, which gives rise to a higher concentration of CO in the products. Consequently, the classical global power-law mechanism is used instead of the Langmuir-Hishelwood mechanism [28, 36].
- The model does not establish different reactivities for the most superficial layer of the particle with the presence of non-graphitized carbon that includes hydrogen radicals and other functional groups and for the innermost structure where formations of graphitized carbon organized in several layers predominate. In this regard, the works of Bhatia and Gupta show that the effect of surface chemistry is not dominant in gasification processes [27].
- Variations in the intrinsic reactivity with the conversion due to catalytic effects related to the presence of alkaline and alkaline-earth elements (AAEM) in this specific biomass are not considered. Potassium is the most active element for char gasification. However, at high temperatures, Si reacts with K to form silicates, acting as an inhibitor and blocking the catalytic effect of K [14,40]. A detailed discussion of the effect of chemical composition and particle size

distribution on barley straw char – CO_2 gasification reaction, including a completed experimental campaign with isothermal and non-isothermal TGA tests at different heating rates and the determination of different indexes that can be used to predict the influence of AAEM on the char gasification reactivity such as the K/Si ratio or the alkali index (AI) has been made in the work by Gil et al. [40].

Based on these hypotheses, the global intrinsic reaction rate of the CO_2 activation process is expressed as follows:

$$\frac{dX}{dt} = k(T)G(P_{CO_2})f(X) \tag{2}$$

in which X is the conversion corresponding to the activation process calculated according to equation (1). The effects of the reaction temperature and partial pressure of the reacting gas (CO_2) in the gas phase are introduced through an apparent reaction rate constant that includes both effects (equation (3)).

$$k(T)G(P_{CO_2}) = k(T, P_{CO_2}) = k_0 e^{-E_a/R_u T} \tag{3}$$

Finally, *f(X)* is the function that describes the changes in the physicochemical properties of the char with conversion. The choice of the conversion model *f(X)* is essential to define the conversion process appropriately. The complexity of the activation process determines this choice since it is affected by the heterogeneous nature of the char structure and the conditions in which the process takes place. Consequently, numerous theoretical and semi-empirical models *f(X)* have been developed to describe this evolution. To determine which model best represents the activation process in this work, a comparative study of the conversion curves obtained by the most representative conversion models in the literature has been carried out: VRM, SCRM, HM and RPM [28].

The VRM and the SCRM are the classical theoretical models in which reactivity decreases monotonically with conversion. The standard semi-empirical n-order HM has also been analyzed, where the value of the reaction order n was fitted by an error minimization procedure over the TGA conversion curves, thus improving the precision in cases where neither VRM nor SCRM describe the process accurately. Finally, among the so-called pore models, the RPM, unlike the previous ones, represents the change in the structure of the char during the growth of the micropores in the initial stages of the activation, which contributes to the increase in specific surface area and thus of reactivity, and the progressive destruction of the pores due to their coalescence by collapse as conversion progresses. In this work, the structural parameter ψ has been determined by regression to the experimental conversion results obtaining a value of 1.75 [41]. Such a low value indicates that pore growth will be insignificant during the reaction, with pore coalescence as the dominant mechanism [42].

Modified versions of the RPM were not considered since the variations introduced in these models are intended to change the conversion curve when there is a maximum reactivity for conversions above 0.393, a characteristic value of catalytic gasification processes [28]. In typical activation processes, the final conversion is low (<0.5), and the maximum reactivity is reached below the 0.393 threshold so that the predictions of the classic RPM are sufficiently accurate, as shown in the validation.

The kinetic parameters have been determined from the isothermal thermogravimetric tests mentioned above, following a non-isoconversional strategy for each model *f(X)*. The integral form of the reaction rate for each model is rearranged into a linear form passing through the origin as shown in Table 5 [43,44]. Then, the slopes of these curves are used to determine the kinetic rate constant k at different temperatures.

Finally, once the kinetic rate constant k for each model at different temperatures has been determined, the apparent activation energy and the pre-exponential factor are obtained from their dependence on temperature using the linear plot of the Arrhenius equation:

$$lnk = ln\ k_0 - \frac{E_a}{R_u T} \tag{4}$$

in which $-E_a/R$ is the slope and lnk_0 is the intercept.

In all cases, a high value of the square of the correlation coefficient ($R^2 > 0.98$) in the linear fit of the Arrhenius plot (Table 6) was obtained. The slope of the curves was constant, confirming the assumption of the pure kinetic regime. Furthermore, it was observed that the reactivity increases at higher temperatures.

Concerning kinetic parameters, the pre-exponential factor refers to the mass loss rate, and the activation energy determines the lowest temperature at which the reaction begins. Consequently, low kinetic parameters indicate high reactivity and mass loss. Kinetic parameters for RPM were found to be lower than those for the other models ($E_{a,VRM}$ $k_{0,VRM} > E_{a,SCRM}$ $k_{0,SCRM} > E_{a,HM}$ $k_{0,HM} > E_{a,RPM}$ $k_{0,RPM}$). These results are consistent with those obtained by other authors [42–44].

Once kinetic parameters were determined, models were validated by comparing the experimental conversion results with the predicted values by the different models. The average relative error over the complete conversion curve was 9.27% (VRM), 10.10% (SCRM), 8.32% (HM), and 4.29% (RPM).

Therefore, the most accurate results have been obtained for the RPM. Moreover, it is the only model that describes the porous structure and allows determining the specific surface area and its evolution during the conversion process according to equation (5) [25].

$$\frac{S}{S_0} = (1-X)\sqrt{1 - \psi\ ln(1-X)} \tag{5}$$

To validate the model in terms of the specific surface area, the values obtained with the RPM were compared with the BET-specific surface area determined experimentally on the activated carbon samples obtained at different conversion times in the horizontal quartz tubular reactor tests. These results, which will be presented later (dashed line in Fig. 5), show that the RPM fails to predict the development of the specific surface area during activation, even if it determines a slight decrease in it with the conversion.

To better understand this result, Fig. 2 shows the influence of the structural parameter on the evolution of the specific surface area. A high value of ψ gives rise to a large surface area evolution due to pore growth. In contrast, a low value of ψ is related to a slight pore growth, being pore coalescence the primary mechanism and, consequently, the specific surface area decreases with conversion [42].

The low value obtained for the structural parameter (1.75) in this work is characteristic of particles with an extensive initial porosity. However, as shown in Table 4, the initial porosity and specific surface

Table 5
The linearized form of the reaction rate equation for each conversion model f(X).

Model	The linearized form of the reaction rate equation
VRM	$k\,t = -ln(1-X)$
SCRM	$k\,t = 3(1-(1-X)^{1/3})$
HB	$k\,t = \frac{1-(1-X)^{(1-n)}}{(1-n)}$
RPM	$k\,t = \frac{2}{\psi}(\sqrt{1-\psi\,ln(1-X)} - 1)$

Table 6
Kinetic parameters for each model considered in this work.

Model	VRM	SCRM	HM	RPM
k_0 (min^{-1})	1.075 E+07	4.181 E+06	2.127 E+06	8.194 E+05
Ea (kJ/mol)	175.2	168.1	161.8	153.8
R^2	0.992	0.987	0.997	0.993

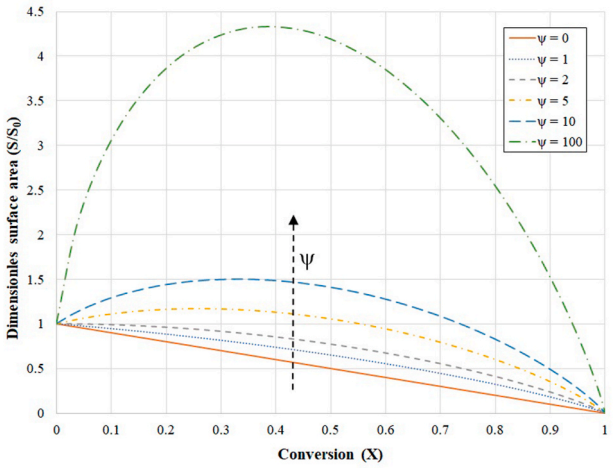

Fig. 2. Influence of the structural parameter in the evolution of the specific surface area.

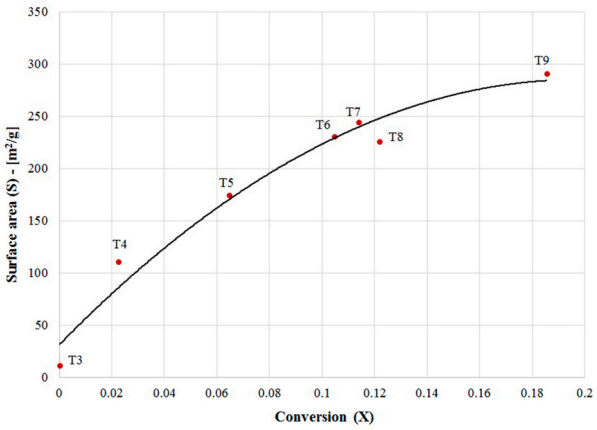

Fig. 3. Evolution of the specific surface area with conversion.

area obtained in the physisorption tests are very low: 0.0113 cm^3/g and 11.59 m^2/g, respectively. Consequently, although the initial char samples present a very low porosity, the structural parameter obtained experimentally and used in the model calculations is characteristic of a very porous structure, predicting a decrease in the specific surface area. At this point, it is worth wondering why an initial char sample with a low porosity presents a small value of the structural parameter characteristic of high porosity structures.

On the one hand, during carbonization, part of the higher molecular weight species ends up re-polymerizing and condensing on the particle's surface, blocking the initial porous structure developed during this pyrolysis stage. In this way, the microporosity obtained in the physisorption test is quite scarce and very narrow (<1 nm), which prevents N_2 diffusion. This explains that although, the BET surface area of the char is initially low, a developed but closed porous structure turns up as the conversion progresses when the species that block the pores are released. This result is, therefore, consistent with obtaining a low structural parameter in the fit of the complete conversion curve and also with the fact that the specific surface area grows during the initial conversion stages, a characteristic of the activated carbon production process.

On the other hand, activation with CO_2 forms two types of new micropores in the structure: those that previously existed but were initially blocked by condensable species and other micropores originating from the gasification reaction. Regardless of the source of this new porosity, the RPM only considers the growth and coalescence of the initially existing pores in the char. That is, it does not consider the formation of new pores.

To sum up, when the RPM is used to determine the evolution of the specific surface in this work, the initial specific surface value is inconsistent with the value of the structural parameter used in the calculations, and the creation of new porosity is not considered.

With the purpose of a deeper understanding of these aspects and experimentally confirming these conclusions, an analysis of the evolution of the internal structure of the char during the conversion has been carried out based on the results of the porosity, specific surface area, and distribution of pore sizes of the activated samples obtained in the tests.

First, Fig. 3 shows the relationship between conversion and specific surface area during the activation process. The specific surface area increases faster in the first conversion stages (approximately linearly until conversion of 0.1), and this growth rate is later attenuated. This result can be interpreted as that, in the beginning, the predominant and almost exclusive mechanism is the formation of new pores due to the release of the species blocking the incipient porosity developed in the previous carbonization process. This is consistent with other works, which state that during activation, carbon dioxide would preferentially react with the heavy tars that plugged the pores in the later pyrolysis stages [34]. As the conversion progresses, and with an increasingly released porosity, the effect of pore growth starts to appear. This is represented by the decrease in the curve slope in Fig. 3. However, in the conversion range in which the activation process occurs, this decrease is insignificant, showing that the formation of new pores is the dominant mechanism against pore growth and coalescence.

Additionally, Fig. 4 shows the evolution of the pore size distribution obtained by DFT from the physisorption tests carried out on the samples obtained at different conversion times: T3 (0 min), T4 (10 min), T5 (20 min), T6 (30 min), T7 (40 min), T8 (50 min) and T9 (60 min). Two distinct regions corresponding to microporosity (~2 nm) and narrow microporosity (<0.5 nm) can be observed. In both cases, as the conversion progresses, there is an increase in the specific surface area (the curves grow vertically). However, the pore size distribution remains practically constant with conversion, which means, there is no significant distribution shift towards larger pore sizes with conversion (shift of the curves to the right). This result confirms that the dominant mechanism is the formation of new pores versus the growth of existing pores. In addition, by presenting such a uniform pore size distribution, it seems reasonable to assume that the porosity that appears is mainly due to the release of species that initially keep the porosity blocked versus the strict formation of new micropores, which would shift the pore size distribution to the left.

It is concluded, therefore, that RPM is adequate to predict the conversion of the char particle in the activation process but not to determine the evolution of the specific surface area, dominated by the appearance

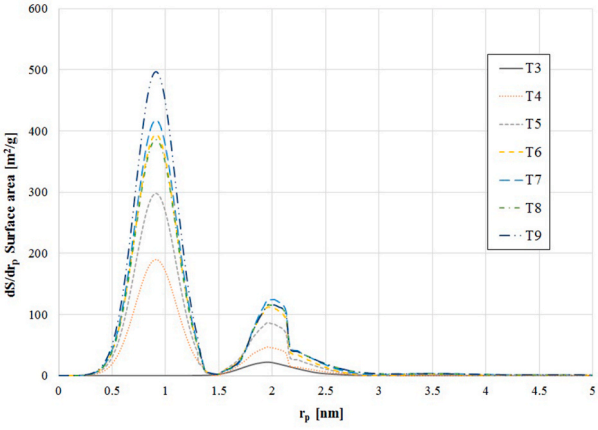

Fig. 4. Evolution of pore size distribution with conversion.

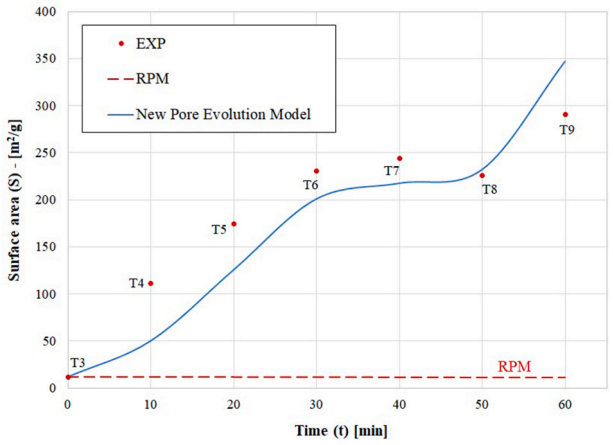

Fig. 5. Variation of surface area with activation time: experimental test results compared to the model approaches: RPM and Pore Evolution Model.

of new pores at the early stages of conversion.

Two modeling alternatives that allow reproducing the evolution of the specific surface area with conversion are considered. The first one consists of using a structural parameter that changes with conversion. It would take high values in the first stages, consistent with an initial low porous char for which the increase in the specific surface due to the growth of the pores dominates, and then progressively decreases with conversion. Examples of this modeling alternative are the proposals of Morimoto et al., 2006 [30] and Fei et al., 2011 [45]. Morimoto et al. already attribute the variation of the structural parameter to the widening of micropores that had not been detected from the BET physisorption tests and to the opening of closed pores that had been blocked by the condensation of species on the surface during pyrolysis. It is then necessary to determine the structural parameter experimentally along the conversion curve (equation (6)), with the added problem that at low conversions, due to the low accessible porosity, the adsorption-desorption curves may not reach equilibrium.

$$\psi_X = \frac{1}{\rho_{S-X}(V_{N2-X} + V_{CO2-X} + V_{C-X})} \tag{6}$$

in which ρ_S is the bulk density of the solid, V_{N2} and V_{CO2} are the pore volume per unit weight obtained by CO_2 and N_2 adsorptions, respectively, and V_C is the pore volume per unit weight corresponding to closed pores.

Fei et al. also observe that the changes in the size of the pores in relation to the change in the specific surface area were small and introduce this behavior through the dependence of the structural parameter on the evolution of the specific surface area and conversion (equation (7)). In this case, the authors use the fractal theory to find characteristic fractal dimensions of the particle that represent its specific surface area. Therefore, additional complexity is introduced into the model.

$$\psi_X = \psi_0 \left(\frac{S_0}{S}\right)\left(1 - \frac{\rho_0 - \rho_{ash}}{\rho_0} X\right) = \psi_0 \sigma^{(D_R - D_0)}\left(1 - \frac{\rho_0 - \rho_{ash}}{\rho_0} X\right) \tag{7}$$

In equation (7), ψ_0 is the initial structure parameter, S and S_0 are the initial and actual reaction surface area of overlapped system per unit volume, respectively, ρ_0 the initial density of the solid, ρ_{ash} the final density of the solid, X conversion, σ the solid molecule radius around the cylindrical pore, and D_R the surface fractal dimension of the particle.

The second modeling alternative, developed in this work, consists of predicting the developed surface due to the formation of new pores and subsequently combining it with determining the variation of the specific surface area predicted by the RPM due to the growth and coalescence of existing pores.

For the development of this new model, the following hypotheses have been considered.

- Char particles of spherical geometry with a particle density ρ_s and an initial surface area per unit volume S_0 determined experimentally over the pyrolyzed samples at 800 °C corresponding to the zero conversion reference (Test 3).
- When the formation of new pores is the dominant mechanism (versus pore growth and coalescence), the mass loss corresponds entirely to the appearance of new pores.

Cylindrical pores are assumed, characterized by the mean pore radius r_{pm} of the pore size distribution (or two mean pore radii characteristic of the microporosity r_{pm1} and narrow microporosity r_{pm2} regions, or more generally by a pore size distribution $f(r_p)$). According to physisorption tests conducted on the activated carbon samples at different levels of conversion, which show that the mean pore size diameter does not change appreciably with time (Fig. 4), mean pore radius r_{pm} (or r_{pm1} and r_{pm2}) is assumed to be constant over the activation stage. Similar results were found by Coloma et al. [34], considering in their model that activation deepens but does not widen the pores. The r_{pm} value used in the calculations corresponds to the activated sample at 800 °C (zero conversion reference – Test 3).

Based on these assumptions, the expression that allows determining the surface developed due to the formation of new pores ΔS_{fp} is obtained as follows (equation (8)):

$$\Delta S_{fp} = \frac{2X}{\rho_s\, r_{pm}\,(1 - X)} \tag{8}$$

If the variation of the specific surface area due to pore growth or their coalescence begins to be significant, the final specific surface is determined considering both effects (equation (9)):

$$S = S_0 + \varphi \Delta S_{fp} + \Delta S_{RPM} \tag{9}$$

in which φ is the relative contribution of the formation of new pores to the total variation of the specific surface area, ΔS_{fp} is the surface area change due to the formation of new pores determined from equation (8), and ΔS_{RPM} the variation of the specific surface area due to the pore growth and coalescence, obtained according to equation (5). The parameter φ, which expresses the instantaneous weight of the formation of new pores in the evolution of the specific surface area, is determined at each time by comparing the actual variation of the specific surface area dS/dX due to the formation of new pores dS_{fp}/dX with the actual variation due to the growth of existing pores dS_{RPM}/dX obtained by the RPM, determined using the actual surface area at the evaluation instant.

The model has been validated with the BET surface area results obtained for the activated carbon samples produced at different activation times in the experimental test campaign. Fig. 5 shows how, unlike RPM, including the formation of new pores mechanism, the new model proposed in this work reasonably predicts the evolution of the specific surface throughout the conversion process. To show more clearly the effect that the introduction of the pore formation mechanism has on the prediction, Fig. 6 shows the relative influence of pore formation on the total surface area developed on the particle. In the range of conditions in which the activation process takes place, the formation of new pores represents more than 90% ($\varphi > 0.9$) of the new specific surface area developed during the process (Fig. 6). These results clearly explain why the new proposed model adequately predicts the evolution of the specific surface area while the RPM that only accounts for the growth and coalescence of the existing pores does not (Fig. 5).

For all the activation tests carried out in the reactor, an average relative error of 14.8% has been reported.

The model is completed by determining the pore size distribution from the specific surface area calculated at a certain conversion level. The pore size distribution presents two maxima: one corresponding to a

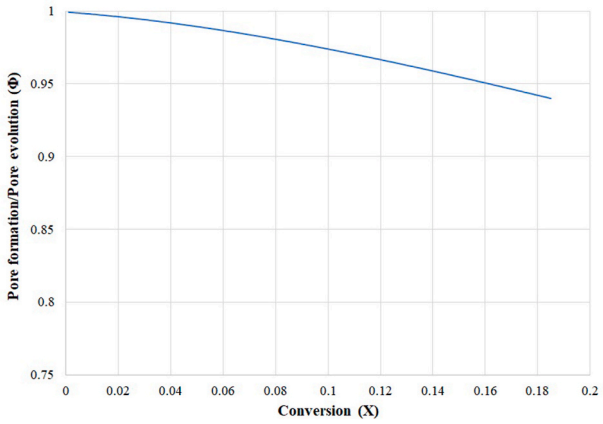

Fig. 6. The relative influence of pore formation and growth/coalescence mechanisms.

mean pore radius around 2 nm and a second maximum in the narrow microporosity region with a pore radius below 1 nm.

In the microporosity region (maximum around 2 nm), the experimental values fit accurately (error <3.4%) to a Gaussian distribution centered on the maximum characteristic value of that region. Meanwhile, in the narrow microporosity region (<1 nm), where the availability of experimental data on the variation of the specific surface is much more limited, the available data have also been fitted to a normal distribution centered on the mean pore radius so that it reproduces the accumulated porosity in that region.

In this way, the characteristic parameters of the corresponding statistical distributions have been obtained from the experimental adsorption data on the activated carbon samples at different conversions (Table 7).

Finally, from these data and assuming that the mean pore radius in each distribution does not change significantly with conversion, it is possible to find the characteristic parameters of each distribution corresponding to a given specific surface by regression.

For the most general case, in which the variation of the surface area due to the growth and coalescence of the existing pores is also considered, the parameter φ introduces to what extent each mechanism affects the variation of the final pore size distribution. Therefore, to include the effect of the variation of the specific surface area due to pore growth and coalescence on the pore size distribution, the variation of the surface area according to the RPM is used. Considering that the RPM hypothesizes that the porous structure is described by cylindrical pores whose total length per unit volume L_E does not change (and what changes is the radius, represented by the distribution function), it is inferred that the variation of mean pore radius of the distribution is proportional to the variation of the surface area as shown in equation (10).

$$\frac{S}{S_0} = \frac{r_{pm}}{r_{pm0}} \tag{10}$$

Therefore, the new pore size distribution, shifted by an abscissa $\delta = r_{pm} - r_{pm0}$, is obtained due to the combined mechanisms of pore formation, growth, and coalescence.

Table 7
Characteristic parameters of the Gaussian distributions for the pore sizes distribution obtained in the activation tests (T3 – T9).

	Narrow microporosity region (<1 nm)			Microporosity region (~2 nm)		
	A_N ($m^2g^{-1}nm^{-1}$)	μ_N (nm)	σ_N (nm)	A_N ($m^2g^{-1}nm^{-1}$)	μ_N (nm)	σ_N (nm)
T3 (t = 0 min)	19.8	1.38	0.22	5.84	2.53	0.23
T4 (t = 10 min)	189.9	0.97	0.19	56.3	1.97	0.18
T5 (t = 20 min)	298.0	0.97	0.19	88.2	1.97	0.18
T6 (t = 30 min)	394.1	0.97	0.19	116.4	1.97	0.18
T7 (t = 40 min)	417.5	0.97	0.19	123.5	1.97	0.18
T8 (t = 50 min)	385.8	0.97	0.19	114.0	1.97	0.18
T9 (t = 60 min)	496.7	0.97	0.19	146.9	1.97	0.18

4. Conclusions

A new reaction model of the physical activation process for the production of activated biocarbon has been developed, which allows predicting -the evolution of the porous structure (surface area, pore volume, and pore size distribution) of a biomass-derived carbonaceous material depending on its physicochemical properties and on conversion for any particular conditions in which the activation process takes place.

For the CO_2 activation process conditions in this work with temperatures below 900 °C and particle sizes below 500 μm, Thiele modulus values below 0.2 have been obtained, establishing the hypothesis of a purely kinetic regime in the modeling. Regarding modeling the gasification reaction's kinetics, Arrhenius-type expressions to express the dependence on temperature and a global power law mechanism on the carbon dioxide concentration have been considered.

Finally, to describe the changes in the physicochemical properties of char during conversion, four of the most widespread theoretical and semi-empirical models in the literature have been evaluated: VRM (volume reaction model), SCRM (shrinking core reaction model), HM (hybrid model) and RPM (random pore model). The determination of the kinetic parameters in each model has been carried out through isothermal TGA tests at five different temperatures (700–900 °C) over the conversion range 0.2–0.8, obtaining a high correlation in the linear fit of the Arrhenius plot ($R^2 > 0.98$) in all cases. In validating the conversion results predicted by the different models with the experimental tests carried out in a tubular heated reactor, the RPM has been revealed as the most accurate model with a global relative error of 4.29%. In comparison, the other three models present a slightly higher relative error: HM (8.32 %), VRM (9.27%), and SCRM (10.10%).

However, the validation of RPM in terms of the specific surface area has shown that it does not correctly predict its evolution, showing, for example, for the conditions analyzed in this work, a decrease in the specific surface area with conversion instead of the remarkable increase in porosity obtained in the activation tests. The causes have been analyzed, and it is concluded that, firstly, the initial value of the specific surface area is not consistent with the value of the structural parameter used in the calculations and, secondly, the RPM does not take into account the creation of new porosity, closed or blocked by condensed species or directly due to the appearance of new pores, which in activation processes is the dominant pore evolution mechanism.

Consequently, a new model has been developed that predicts the specific surface area created due to the formation of new pores. Subsequently, it is combined with determining the variation of the specific surface area indicated by RPM due to the growth and coalescence of existing pores. The validation of the model with the BET surface area results obtained for the activated carbon samples produced at different activation times shows that the new pore evolution model proposed in this work adequately predicts the specific surface area throughout the activation process (relative error of 14.8%). This model, which has been

validated for barley straw, can be adapted for other types of biomass in the future.

The model is completed by determining the pore size distribution from the specific surface area calculated at a certain conversion level. The experimental values accurately fit a Gaussian distribution in the microporosity zone (maximum around 2 nm). In comparison, in the narrow microporosity zone (<1 nm), where the availability of experimental data on the variation of the specific surface area is much more limited, the available data have also been fitted to a normal distribution centered on the mean pore radius so that it reproduces the accumulated porosity in that region.

The developed model allows modeling the evolution of the porous structure of a biomass material, in terms of the quantity and distribution of pore sizes during the activation process, which mainly determines the adsorption capacity of an AC, obtaining a potent tool for analyzing and optimizing the operation variables of industrial reactors as well as the possibility of extending the study to other precursor materials.

CRediT authorship contribution statement

Javier Pallarés Ranz: Conceptualization, Data curation, Formal analysis, Funding acquisition, Investigation, Methodology, Project administration, Resources, Software, Supervision, Validation, Visualization. **Antonia Gil:** Conceptualization, Data curation, Formal analysis, Investigation, Writing – review & editing. **Cristóbal Cortés:** Conceptualization, Investigation, Writing – review & editing. **Inmaculada Arauzo:** Conceptualization, Investigation, Writing – review & editing.

Declaration of competing interest

The authors declare that they have no known competing financial interests or personal relationships that could have appeared to influence the work reported in this paper.

Acknowledgments

Funding sources comes from two different projects: 1.) Project: RTI2018-095349-A-I00 funded by the Spanish Ministry of Science, Innovation, and Universities under the RETOS-INVESTIGACIÓN program and co-financed by the European Union with the European Research and Developments funds.2.) Project: TED2021-131397B–I00 funded by the funded by the Spanish Ministry of Science and Innovation under the PROYECTOS ORIENTADOS A LA TRANSICIÓN ECOLÓGICA Y A LA TRANSICIÓN DIGITAL program and co-financed by the European Union with the NextGeneration recovery planThe other organizations that appear in this acknowledgments sections refers to external collaborations in the physical and chemical characterization of the raw materials and activated carbons. These entities are the Servicio General de Apoyo a la Investigación-SAI (University of Zaragoza), the Instituto de Carboquímica (ICB-CSIC) and the Instituto de Nanociencia de Aragón.

References

[1] European Commission, Directorate-General for Energy, Energy: Roadmap 2050, Publications Office, 2012, https://doi.org/10.2833/10759.
[2] X.F. Tan, S.B. Liu, Y.G. Liu, Y.L. Gu, G.M. Zeng, X.J. Hu, X. Wang, S.H. Liu, L. H. Jiang, Biochar as potential sustainable precursors for activated carbon production: multiple applications in environmental protection and energy storage, Bioresour. Technol. 227 (2017) 359–372, https://doi.org/10.1016/j.biortech.2016.12.083.
[3] Y. Yin, S.B. Liu, Q. Liu, J. Wang, Y. Zhao, Recent insights in synthesis and energy storage applications of porous carbon derived from biomass waste: a review, Int. J. Hydrogen Energy 47 (2022) 39338–39363, https://doi.org/10.1016/j.ijhydene.2022.09.121.
[4] L. Zubizarreta, A. Arenillas, J.J. Pis, Carbon materials for H2 storage, Int. J. Hydrogen Energy 34 (2009) 4575–4581, https://doi.org/10.1016/j.ijhydene.2008.07.112.
[5] M. Mohan, V.K. Sharma, E.A. Kumar, V. Gayathri, Hydrogen storage in carbon materials-A review, Energy Storage 1 (2019) 1–26, https://doi.org/10.1002/est2.35.
[6] E.I. Epelle, K.S. Desongu, W. Obande, A.A. Adeleke, P.P. Ikubanni, J.A. Okolie, B. Gunes, A comprehensive review of hydrogen production and storage: a focus on the role of nanomaterials, Int. J. Hydrogen Energy 47 (2022) 20398–20431, https://doi.org/10.1016/j.ijhydene.2022.04.227.
[7] H. Badenhorst, A review of the application of carbon materials in solar thermal energy storage, Sol. Energy 192 (2019) 35–68, https://doi.org/10.1016/j.solener.2018.01.062.
[8] A. Stonehouse, Ch Abeykoon, Thermal properties of phase change materials reinforced with multi-dimensional carbon nanomaterials, Int. J. Heat Mass Tran. 183 (2022) 122166, https://doi.org/10.1016/j.ijheatmasstransfer.2021.122166.
[9] R.K. Mishra, K. Verma, V. Mishra, B. Chaudhary, A review on carbon-based phase change materials for thermal energy storage, J. Energy Storage 50 (2022) 104166, https://doi.org/10.1016/j.est.2022.104166.
[10] B.K. Choure, T. Alam, R. Kumar, A review on heat transfer enhancement techniques for PCM based thermal energy storage system, J. Energy Storage 72 (2023) 108161, https://doi.org/10.1016/j.est.2023.108161.
[11] Y. Zhang, H. Pan, Q. Zhou, K. Liu, W. Ma, S. Fan, Biomass-derived carbon for supercapacitors electrodes – a review of recent advances, Inorg. Chem. Commun. 153 (2023) 110768, https://doi.org/10.1016/j.inoche.2023.110768.
[12] S.A. Bhat, V. Kumar, S. Kumar, A.E. Atabani, I.A. Badruddin, K.J. Chae, Supercapacitors production from waste: a new window for sustainable energy and waste management, Fuel 337 (2023) 127125, https://doi.org/10.1016/j.fuel.2022.127125.
[13] D. Dong, Y. Xiao, Recent progress and challenges in coal-derived porous carbon for supercapacitor applications, Chem. Eng. J. 470 (2023) 144441, https://doi.org/10.1016/j.cej.2023.144441.
[14] J. Pallarés, A. González-Cencerrado, I. Arauzo, Production and characterization of activated carbon from barley straw by physical activation with carbon dioxide and steam, Biomass Bioenergy 115 (2018) 64–73, https://doi.org/10.1016/j.biombioe.2018.04.015.
[15] E.E. Petersen, Reaction of porous solids, AIChE J. 3 (1957) 443–448, https://doi.org/10.1002/aic.690030405.
[16] K. Hashimoto, P.L. Silveston, Gasification: Part I. Isothermal, kinetic control model for a solid with pore size distribution, AIChE J. 19 (1973) 259–268, https://doi.org/10.1002/aic.690190209.
[17] K. Hashimoto, K. Miura, F. Yoshikawa, I. Imai, Change in pore structure of carbonaceous materials during activation and adsorption performance of activated carbon, Ind. Eng. Chem. Process Des. Dev. 18 (1979) 72–80, https://doi.org/10.1021/i260069a010.
[18] K. Miura, K. Hashimoto, A model representing the change of pore structure during the activation of carbonaceous materials, Ind. Eng. Chem. Process Des. Dev. 23 (1984) 138–145, https://doi.org/10.1021/i200024a023.
[19] G.A. Simons, M.L. Finson, The structure of coal char: Part I. Pore branching, Combust. Sci. Technol. 19 (1979) 217–225, https://doi.org/10.1080/00102207908946882.
[20] G.A. Simons, The structure of coal char: Part II. Pore combination, Combust. Sci. Technol. 19 (1979) 227–235, https://doi.org/10.1080/00102207908946883.
[21] G.A. Simons, The pore tree structure of porous char, in: 19th Symposium (International) on Combustion, The Combustion Institute, 1982, pp. 1067–1076, https://doi.org/10.1016/S0082-0784(82)80282-8.
[22] G.R. Gavalas, A random capillary model with application to char gasification at chemically controlled rates, AIChE J. 26 (1980) 577–585, https://doi.org/10.1002/aic.690260408.
[23] S.K. Bhatia, D.D. Perlmutter, A random pore model for fluid-solid reactions: I. Isothermal, kinetic control, AIChE J. 26 (1980) 379–386, https://doi.org/10.1002/aic.690260308.
[24] S.K. Bhatia, D.D. Perlmutter, A random pore model for fluid-solid reactions: II. Diffusion and transport effects, AIChE J. 27 (1981) 247–254, https://doi.org/10.1002/aic.690270211.
[25] J.L. Su, D.D. Perlmutter, Evolution of pore volume distribution during gasification, AIChE J. 30 (1984) 967–973, https://doi.org/10.1002/aic.690300612.
[26] S.K. Bhatia, B.J. Vartak, Reaction of microporous solids: the discrete random pore model, Carbon 34 (1996) 1383–1391, https://doi.org/10.1016/S0008-6223(96)00080-2.
[27] J.S. Gupta, S.K. Bhatia, A modified discrete random pore model allowing for different initial surface reactivity, Carbon 38 (2000) 47–58, https://doi.org/10.1016/S0008-6223(99)00095-0.
[28] P. Lahijani, Z.A. Zainal, M. Mohammadi, A.R. Mohamed, Conversion of the greenhouse gas CO2 to the fuel gas CO via the Boudouard reaction: a review, Renew. Sustain. Energy Rev. 41 (2015) 615–632, https://doi.org/10.1016/j.rser.2014.08.034.
[29] R.P.W.J. Struis, C. von Scala, S. Stucki, R. Prins, Gasification reactivity of charcoal with CO2. Part I: conversion and structural phenomena, Chem. Eng. Sci. 57 (2002) 3581–3592, https://doi.org/10.1016/S0009-2509(02)00254-3.
[30] T. Morimoto, T. Ochiai, S. Wasaka, H. Oda, Modeling on pore variation of coal chars during CO2 gasification associated with their submicropores and closed pores, Energy Fuel. 20 (2006) 353–358, https://doi.org/10.1021/ef0502296.
[31] Y. Zhang, M. Ashizawa, S. Kajitani, K. Miura, Proposal of a semi-empirical kinetic model to reconcile with gasification reactivity profiles of biomass chars, Fuel 87 (2008) 475–481, https://doi.org/10.1016/j.fuel.2007.04.026.
[32] H. Fei, L. Sun, S. Hu, J. Xiang, Y. Song, B. Wang, G. Chen, The combustion reactivity of coal chars in oxyfuel atmosphere: comparison of different random pore models, J. Anal. Appl. Pyrol. 91 (2011) 251–256, https://doi.org/10.1016/j.jaap.2011.02.014.

[33] J.L. Zhang, G.W. Wang, J.G. Shao, H.B. Zuo, A modified random pore model for the kinetics of char gasification, Bioresources 9 (2014) 3497–3507, https://doi.org/10.15376/biores.9.2.3497-3507.
[34] A. Colomba, F. Berruti, C. Briens, Model for the physical activation of biochar to activated carbon, J. Anal. Appl. Pyrol. 168 (2022) 105769, https://doi.org/10.1016/j.jaap.2022.105769.
[35] E.W. Thiele, Relation between catalytic activity and size of particle, Ind. Eng. Chem. 31 (1939) 916–920, https://doi.org/10.1021/ie50355a027.
[36] A. Gómez-Barea, P. Ollero, C. Fernández-Baco, Diffusional effects in CO2 gasification experiments with single biomass char particles. 1. Experimental investigation, Energy Fuel. 20 (2006) 2202–2210, https://doi.org/10.1021/ef050365a.
[37] T. Mani, N. Mahinpey, P. Murugan, Reaction kinetics and mass transfer studies of biomass char gasification with CO2, Chem. Eng. Sci. 66 (2011) 36–41, https://doi.org/10.1016/j.ces.2010.09.033.
[38] W. Huo, Z. Zhou, X. Chen, Z. Dai, G. Yu, Study on CO2 gasification reactivity and physical characteristics of biomass, petroleum coke and coal chars, Bioresour. Technol. 159 (2014) 143–149, https://doi.org/10.1016/j.biortech.2014.02.117.
[39] Y. Liu, J. Qu, X. Wu, K. Zhang, Y. Zhang, Reaction kinetics and internal diffusion of Zhundong char gasification with CO2, Front. Chem. Sci. Eng. 15 (2021) 373–383, https://doi.org/10.1007/s11705-020-1949-2.
[40] Gil, J. Pallarés, I. Arauzo, C. Cortés, Pyrolysis and CO2 gasification of barley Straw: effect of particle size distribution and chemical composition, Powder Technol. 424 (2023) 118539, https://doi.org/10.1016/j.powtec.2023.118539.
[41] R.C. Everson, H.W.J.P. Neomagus, R. Kaitano, R. Falcon, V.M. du Cann, Properties of high ash coal-char particles derived from inertinite-rich coal: II. Gasification kinetics with carbon dioxide, Fuel 87 (2008) 3403–3408, https://doi.org/10.1016/j.fuel.2008.05.019.
[42] L. Lin, M. Strand, Investigation of the intrinsic CO2 gasification kinetics of biomass char at medium to high temperatures, Appl. Energy 109 (2013) 220–228, https://doi.org/10.1016/j.apenergy.2013.04.027.
[43] K. Kirtania, S. Bhattacharya, CO2 Gasification kinetics of algal and woody char procured under different pyrolysis conditions and heating rates, Sustainable Chemistry & Engineering 3 (2015) 365–373, https://doi.org/10.1021/sc500777u.
[44] A.N. Izaharuddin, M.C. Paul, K. Yoshikawa, S. Theppitak, X. Dai, Comprehensive kinetic modeling study of CO2 gasification of char derived from food waste, Energy Fuel. 34 (2020) 1833–1895, https://doi.org/10.1021/acs.energyfuels.9b03937.
[45] H. Fei, S. Hu, J. Xiang, L. Sun, P. Fu, G. Chen, Study on coal chars combustion under O2/CO2 atmosphere with fractal random pore model, Fuel 90 (2011) 441–448, https://doi.org/10.1016/j.fuel.2010.09.027.